LAWRENCE
LIVERMORE
NATIONAL
LABORATORY

Combining nanocalorimetry and dynamic transmission electron microscopy for in situ characterization of materials processes under rapid heating and cooling

M. D. Grapes, T. LaGrange, L. H. Friedman, B. W. Reed, G. H. Campbell, T. P. Weihs, D. A. LaVan

May 27, 2014

Disclaimer

This document was prepared as an account of work sponsored by an agency of the United States government. Neither the United States government nor Lawrence Livermore National Security, LLC, nor any of their employees makes any warranty, expressed or implied, or assumes any legal liability or responsibility for the accuracy, completeness, or usefulness of any information, apparatus, product, or process disclosed, or represents that its use would not infringe privately owned rights. Reference herein to any specific commercial product, process, or service by trade name, trademark, manufacturer, or otherwise does not necessarily constitute or imply its endorsement, recommendation, or favoring by the United States government or Lawrence Livermore National Security, LLC. The views and opinions of authors expressed herein do not necessarily state or reflect those of the United States government or Lawrence Livermore National Security, LLC, and shall not be used for advertising or product endorsement purposes.

Combining nanocalorimetry and dynamic transmission electron microscopy for *in situ* characterization of materials processes under rapid heating and cooling

Michael D. Grapes[1,2,a)], Thomas LaGrange[3], Lawrence H. Friedman[2], Bryan W. Reed[3], Geoffrey H. Campbell[3], Timothy P. Weihs[1,b)], David A. LaVan[2,c)]

[1] *Department of Materials Science and Engineering, Johns Hopkins University, Baltimore, Maryland 21218, USA*

[2] *Materials Measurement Science Division, Material Measurement Laboratory, National Institute of Standards and Technology, Gaithersburg, Maryland 20899, USA*

[3] *Condensed Matter and Materials Division, Lawrence Livermore National Laboratory, Livermore, California 94550, USA*

a) **mgrapes1@jhu.edu,** b) **david.lavan@nist.gov,** c) **weihs@jhu.edu**

Abstract

Nanocalorimetry is a chip-based thermal analysis technique capable of analyzing endothermic and exothermic reactions at very high heating and cooling rates. Here we couple a nanocalorimeter with an extremely fast *in situ* microstructural characterization tool to identify the physical origin of rapid enthalpic signals. More specifically, we describe the development of a system to enable *in situ* nanocalorimetry experiments in the dynamic transmission electron microscope (DTEM), a time-resolved TEM capable of generating images and electron diffraction patterns with exposure times of 30 ns to 500 ns. The full experimental system consists of a modified nanocalorimeter sensor, a custom-built *in situ* nanocalorimetry holder, a data acquisition system, and the DTEM itself, and is capable of thermodynamic and microstructural characterization of reactions over a range of heating rates (10^2 K/s to 10^5 K/s) accessible by conventional (DC) nanocalorimetry. To establish its ability to capture synchronized calorimetric and microstructural data during rapid transformations, this work describes measurements on the melting of an aluminum thin film. We were able to identify the phase transformation in both the nanocalorimetry traces and in electron diffraction patterns taken by the DTEM. Potential applications for the newly-developed system are described and future system improvements are discussed.

I. Introduction

Since its introduction in 1995[1], the technique known as "nanocalorimetry" has found increasingly widespread use in materials research, particularly with the development and use of nanomaterials with microstructural scales below 100 nm. As the name suggests, nanocalorimetry enables thermal analysis on very small samples (typically less than 1 µg) and measurements of correspondingly small energy releases or absorptions (sensitivities of $\approx$ 1 nJ/K are typical). Examples include the melting of thin films and nanoparticles[2–5], the characterization of interfacial reactions between thin films[6,7], and the efficient assessment of combinatorial libraries[8–10].

Traditional nanocalorimeters are based on microfabricated sensors with extraordinary sensitivity achieved by fabricating the active region of the sensor on a very thin silicon nitride membrane to minimize the sensor's heat capacity. This design also typically enables the sensor to achieve increased heating rates over those available in conventional calorimetric techniques such as differential scanning calorimetry (DSC) or differential thermal analysis (DTA). For example, the sensor used in this work is capable of heating as quickly as 10^5 K/s and cooling at rates up to 10^4 K/s. There are a number of benefits to performing experiments at high rates. From an operational perspective, rapid heating minimizes the contribution of heat losses during the heating step so that the nanocalorimeter approximates an adiabatic system[2]. In addition, traditional analysis of nanocalorimetry experiments relies on deviations in the heating rate of the sensor when reactions occur, and these are only measurable when the device is operated quickly. This is the origin of the lower bound on heating rate for nanocalorimetry, which varies based on the magnitude of the reaction in the sample but is typically around 500 K/s. Another benefit to high heating and cooling rates is the short duration of experiments compared to traditional calorimetry (e.g. 20 minutes for a differential scanning calorimetry experiment vs. < 1 s for the same experiment in the nanocalorimeter). Finally, many phase transformations exhibit some rate-dependence when driven at high speeds. The high cooling rates available in the nanocalorimeter have been used to study the glass transition in Ni-Ti-Zr[8] and Au-Cu-Si[10] bulk metallic glasses and polymer[11] samples, and to study recalescence in solidifying aluminum thin films[4]. Recent work has also investigated the heating-rate-dependence of the exothermic formation reaction between Ni and Al[7] using nanocalorimetry.

The best way to characterize dynamic processes experimentally is through *in situ* techniques which allow the state of the system to be observed in real time. High heating and cooling rates present a notable challenge in this regard as they place stringent speed requirements on the characterization tools that can be used. In particular, for traditional nanocalorimetry conventional characterization tools like x-ray diffraction and transmission electron microscopy (TEM) operate on time scales that are impractically slow for *in situ* investigation. There are two solutions to this dilemma: (1) reduce the heating and cooling rates or (2) couple the nanocalorimeter with a technique capable of characterization on much shorter timescales.

The first approach is viable as long as changing the heating rate does not impact the scientific relevance of the investigation. For example, in 2005 Zhang *et al.* showed that *in situ* nanocalorimetry was possible in a conventional TEM, albeit at too low a rate (120 K/s) to measure any properties aside from temperature[5]. The technique known as AC nanocalorimetry has been developed to extend heat capacity measurements to very low heating rates.[12–14] Recently, Vlassak and co-workers have successfully coupled this technique with x-ray synchrotron radiation[15,16] to perform *in situ* characterization at heating rates up to 300 K/s.

For studies in which high heating and cooling rates are important, we describe the design and implementation of a system that couples a nanocalorimeter with high-speed microstructural characterization using the dynamic transmission electron microscope (DTEM). The DTEM is a time-resolved TEM that was developed at Lawrence Livermore National Laboratory. It is capable of sub-μs temporal resolution[17–19] and has been used to study a variety of materials processes at their native timescales including martensitic transformations[20,21], melting and recrystallization[22–28], and exothermic reaction propagation[29,30]. While the nanocalorimetry + DTEM system is theoretically capable of characterizing reactions up to the maximum heating rate of the nanocalorimeter sensor, here we apply the system to study aluminum melting at heating rates of $\approx 10^4$ K/s.

While the new *in situ* nanocalorimetry system combines two well-established techniques, practical implementation required the creation or modification of several critical components.

This work outlines the design of these components and the time sensitive interactions between the nanocalorimeter and the DTEM. In Section II, we describe the design and interaction of the system's various components. Sections III and IV present the first results obtained with the system, studying the melting of an aluminum thin film heated at $\approx 10^4$ K/s. Section V describes future applications and improvements that can be made to the system.

II. Design of Critical System Components

The integrated nanocalorimeter and DTEM system relies upon a combination of new and existing instrumentation, as illustrated in Fig. 1. The sample is deposited on a calibrated nanocalorimeter sensor which is then clamped into a custom-built TEM holder. A 200 kS/s data acquisition system and accompanying software run the nanocalorimetry experiment and interface with the timing electronics of the DTEM to coordinate the capture of an electron image or diffraction pattern at the appropriate time during the experiment. The design of these components is described in more detail in the sub-sections below.

A. Nanocalorimeter Sensors

The nanocalorimeters used for the *in situ* DTEM system are based on the original design by Allen and coworkers[2], updated for use in TEM studies. Each nanocalorimeter is a small silicon chip measuring roughly 0.55 cm x 1.41 cm. The chips are fabricated on 100-mm-diameter Si wafers and then cleaved apart for individual use. A schematic cross-section and micrograph of a typical sensor are shown in Fig. 2. The active region of each sensor consists of a 50 nm thick, 0.5 mm wide Pt heater strip supported by a 150-nm-thick silicon nitride membrane. Two voltage probes make contact with the heater strip with a spacing of 3.7 mm (prior designs have had a spacing of 5.7 mm). The section of the heater between the voltage probes defines the "measurement area" of the nanocalorimeter sensor, where temperature is actively monitored and sample changes are detected. The front side metal layer is fabricated by evaporation and liftoff, and the silicon nitride membrane is created by anisotropic Si etching from the backside using potassium hydroxide. The sample is typically deposited onto the back surface of the silicon nitride directly below the heater, as depicted in Fig. 2a.

The heater strip also serves as the temperature sensor in this nanocalorimeter. The sample is heated by flowing current through the heater strip (from I^+ to I^- in Fig. 2b). The instantaneous

current flowing through the strip is determined by measuring the voltage drop across a precision current sensing resistor in series with the heater and calculating the current in the loop, I, from the voltage drop and sense resistance:

$$I = \Delta V_{sense} / R_{sense} \tag{1}$$

where ΔV_{sense} is the voltage drop across the current sensing resistor and R_{sense} is its resistance. Simultaneously, the voltage drop across the measurement area of the sensor is measured by the voltage probes V^+ and V^-. The resistance of the measurement area, R_{MA}, is calculated by:

$$R_{MA} = \Delta V_{MA} / I \tag{2}$$

where $\Delta V_{MA} = V^+ - V^-$ is the voltage drop across the measurement area and I is the current from Eq. 1. If the temperature vs. resistance relationship of the platinum strip is known, the temperature in the measurement area, T_{MA}, can be calculated as

$$T_{MA} = T_{calib}(R_{MA}) = C_0 + C_1 R_{MA} + C_2 R_{MA}^2 + \cdots \tag{3}$$

where R_{MA} is the resistance from Eq. 2 and T_{calib} is a $2^{nd} - 4^{th}$ order polynomial fit to resistance vs. temperature calibration data. Each sensor is individually stabilized and calibrated using an optical technique detailed previously[31]. T_{MA} (Eq. 3) is one of two basic outputs in a nanocalorimetry experiment. The other is the power applied to the measurement area, P_{MA}, which is calculated as

$$P_{MA} = I \Delta V_{MA} \tag{4}$$

From these two basic outputs, the effective heat capacity of the measurement area (not accounting for heat losses) can be calculated from the power and the heating rate (time-derivative of temperature) as

$$C_{p,MA} = \frac{P_{MA}}{dT_{MA}/dt} \tag{5}$$

In preparation for these experiments, the nanocalorimeter sensor was modified to improve the temperature uniformity of the measurement area and create electron transparent regions for TEM observation. Temperature uniformity was enhanced by reducing the spacing between the voltage probes to limit the effect of longitudinal temperature gradients (in the current design this spacing is 3.7 mm, while previous sensors used 5.7 mm). To provide regions of electron transparency,

three 100 µm x 100 µm square holes were added in the center of the platinum strip (visible in Fig. 2b). Platinum scatters electrons quite strongly, so even though the Pt film is only 50 nm thick it would be very difficult to study the specimen through it. In contrast, the silicon nitride is amorphous and relatively electron-transparent so it was left intact to ensure adequate support for the sample.

Temperature uniformity across the measurement area is a common metric by which heater geometries are assessed. While a tighter temperature distribution does not necessarily improve the accuracy of the mean temperature of the sensor, it does enable it to measure sharper endothermic and exothermic peaks. In order to compare the performance of the new design to the conventional nanocalorimeter[2,4] in this regard and to assess the capabilities of future designs, we performed finite element analysis of the temperature distribution within the measurement area for each. Four designs were tested as enumerated in Table I. The nanocalorimeter used in earlier work corresponds to Design A while the sensors used in the present investigation employed Design C.

The silicon nitride membrane was simulated as having negligible electrical conductivity and negligible black-body emissivity (consistent with observation via thermal imaging and previous work[32]). The Pt conductor was simulated with a temperature-dependent electrical conductivity based on measurements from similar platinum samples. Table II shows the temperature-dependent emissivity used for platinum along with the other material properties used in the model. In the simulations the outer-edges of the silicon nitride membrane were held at room temperature (295.15 K) to simulate the high thermal conductivity of the Si substrate, and the ends of the Pt conductor were assumed to have a uniform current density. The applied current in the model was increased until the measurement area of the Pt reached an average temperature of 939 K. Simulations were performed taking advantage of the 4-fold geometric symmetry. Quadratic wedge-shaped elements were used throughout. Numerical convergence was verified using mesh-density halving. A mesh seed spacing of 25 µm was used throughout the plane of the membrane and the conductor for the simulation of the original nanocalorimeter design. For the new design simulation, a biased mesh seed spacing was used that tended to 2.5 µm in and around the holes. Two layers of elements were used in the plane for each material. These results were

6

compared to a mesh-halved result using a mesh seed spacing of 5 μm to 50 μm and a single element layer for each material, resulting in approximately one-eighth the number of elements. There were no significant differences in the results between the two mesh resolutions. All physical constants were rescaled using dimensional analysis so that entered material properties were of order unity for better numerical behavior.

The simulation results were quantified by extracting temperatures from a uniform grid of points on the Pt surface. Fig. 3 shows contour plots and histograms that compare the temperature distribution within the measurement area for each design. The standard deviations of the distributions are 11.7 K (n = 1859 grid points) for Design A, 3.21 K (n = 1209 grid points) for Design B, 8.24 K (n = 1185 grid points) for Design C, and 3.25 K (n = 1207 grid points) for Design D. Comparing Design A to Design B reveals the improvement in temperature uniformity that can be achieved simply by reducing the length of the measurement area. The effect of adding holes (Designs C and D) is to broaden this distribution due to current concentration around the hole edges, but we see that for sufficiently small holes (Design D) the broadening is minimal. As noted above the sensors used in this work employed Design C. Future work will implement the smaller hole size in Design D to take advantage of that design's improved temperature uniformity.

B. *In Situ* Nanocalorimetry TEM Holder

We designed and fabricated a custom TEM holder for the nanocalorimeter sensor. The basic design requirements for the holder were (a) mechanical compatibility with the goniometer and column of the JEOL 2000FX platform upon which the DTEM is based, (b) a mechanism for stable and repeatable positioning of the nanocalorimeter sensor in the electron beam, (c) the ability to make reliable electrical connections to the pads on the sensor, and (d) vacuum-tight electrical connections to transfer these electrical signals to the external environment. To ensure compatibility with the JEOL 2000FX goniometer the limiting dimensions of the custom holder were adapted from a JEOL EM-BST double-tilting holder. The sensor and the associated electrical connections at the tip had to fit within a 5.1 mm thickness. The bulk of the holder was machined from brass to ensure that it would be non-magnetic – unintended magnetic fields in the TEM can deflect electrons and degrade image quality. Fig. 4a shows the completed holder.

Perhaps the most critical component of the holder is the mechanism for mounting the nanocalorimeter sensor and making electrical connections to it. The mount must be stable (not prone to vibration or drift) and reliable (able to maintain its function over many load/unload cycles). In addition, for TEM it is important that the sample be positioned as close as possible to the rotation axis of the holder. This minimizes the z-adjustment required to place the sample at the eucentric height of the TEM, a critical condition for quantitative analysis of diffraction patterns and generally consistent imaging. With all of these requirements in mind we designed the holder to use a face-down mounting approach. The sensor cavity was designed as shown in Fig. 4c and consists of a 5.84 mm x 14.48 mm rectangular pocket with 1.52 mm circular cutouts in the corners to allow for extra material left over after chip cleavage. It was machined to a depth of 64 μm below the mid-plane of the holder. The remaining thickness is taken up by 64-μm-thick polyimide tape, also visible in Fig. 4c, which is applied to insulate the metal contact pads on the surface of the sensor from incidental contact to the brass holder. Since the sample sits on the silicon nitride membrane (see Fig. 2a) it is essentially flush with the top surface of the sensor. Thus, the sample is positioned almost exactly at the rotation axis of the holder when the sensor is clamped down. The face-down approach ensures that the sample is in the same position for every measurement regardless of variations in the thickness of the silicon wafer. A clamping block secured by two screws allows the user to apply just enough force to ensure that the sensor is flush with the bottom surface and stable – excessive clamping force can break the silicon chip. A photograph of a loaded, clamped sensor is shown in Fig. 4d.

Since the nanocalorimeter sensor is often replaced, a rapid and reliable way to make electrical connections to it was needed. The space available in the JEOL EM-BST form factor allowed the use of commercially available ultra-low-profile spring pins (#0965, Mill-Max Mfg. Corp.). These pins measure 2.54 mm at rest and 1.93 mm when fully compressed. Four spring pins were soldered to a 0.5 mm thick printed circuit board that was mounted to the underside of the holder tip. The board positions the spring pins directly below the sensor cavity. The spring pins protrude up beyond the bottom of the sensor cavity as shown in Fig. 4c if no sensor is loaded. When a sensor is clamped in place, the four contact pads (see Fig. 2b) make contact with the four spring pins and compress them to form a reliable electrical connection.

Electrical connections from the printed circuit board at the holder tip to the auxiliary electronics in the breakout box were made using UT-34 micro-coaxial cable (Micro-Coax, Inc.). These cables have a solid copper outer shield, a PTFE insulating sheath, and a solid copper inner conductor approximately 200 µm in diameter. The solid outer shield greatly simplifies the creation of a vacuum feedthrough for the cables as an air-tight seal can be formed simply by passing them through a small hole and filling the gaps with solder. This also grounds the outer shield to provide noise shielding for the signals carried on the inner conductor. The micro-coaxial cables and vacuum seal are visible at the holder tip in Fig. 4a, and in the breakout box in Fig. 4b.

The final component of the *in situ* nanocalorimetry holder is the auxiliary electronics system housed in the breakout box, shown in Fig. 4b. Besides providing an intermediate interface between the micro-coaxial cables coming from the nanocalorimeter and the BNC cables that transfer signals to the data acquisition system, the auxiliary electronics also house two components which are essential for nanocalorimeter operation: (1) a buffer amplifier to supply the necessary current, and (2) selectable current sensing resistors to measure the current flowing through the heater. The buffer amplifier (Burr-Brown BUF634) is necessary because the digital-to-analog converter used to generate the heating waveform is not designed to drive a low impedance circuit like the nanocalorimeter heater, which typically has a resistance ranging from 50 Ω to 140 Ω. The extra power for the amplifier is provided by a +/- 15 VDC power supply (Agilent 3630A). For current measurement, the *in situ* nanocalorimeter holder features a selection of sense resistors (10 Ω, 25 Ω, 50 Ω, 75 Ω, and 100 Ω) for increased measurement flexibility. Higher sense resistance values result in less noise in the current measurement but limit the total power that can be delivered to the sensor.

C. Data Acquisition System

Because the resolution of the nanocalorimeter output signals (Eq. 3-5) is directly related to the resolution with which the raw voltage signals can be measured, the most critical design parameter for the data acquisition system was to include high-precision analog-to-digital converters. Other priorities were ruggedness, portability, and the ability to easily operate the system from software. The data acquisition system uses a 4-slot PXI Express chassis (NI PXIe-1071) with an embedded controller (NI PXIe-8133) and two high-precision dynamic signal

analysis cards (NI PXI-4461 and NI PXI-4462). This system is capable of simultaneously generating 2 analog outputs and measuring 6 analog inputs with 24-bit resolution at speeds up to 204.8 kHz, sufficient for nanocalorimeter operation. The PXI platform also provides dedicated timing signals and triggering lines so that signal generation and measurement tasks can be precisely synchronized with each other and external equipment like the DTEM.

The embedded controller runs Windows 7 and LabVIEW and is used to program and perform tasks using the system. A custom LabVIEW virtual instrument (VI) was developed for the nanocalorimetry system to streamline both the execution of experiments and the management of data. The general design strategy was to create a single entry-point for all nanocalorimeter operations and introduce specific functionality into an array of subVIs that are called by the primary VI. A high-level diagram of this organization scheme is shown in Fig. 5. Data management is achieved in this approach by assigning each nanocalorimeter sensor a unique identifier and corresponding storage space and asking the user to specify the "working" sensor in the primary VI before running any subVIs. If the working sensor is specified, the locations of all files specific to that sensor are automatically passed to the subVIs when they are called allowing these VIs to read or modify that sensor's properties as necessary and store all new files to the same location. The centralized organization scheme also helps to maintain an efficient workflow because the primary VI only allows the user to launch a subVI when it detects that all previous steps in the workflow have been completed. For example, since measurement data cannot be processed unless a sensor has been calibrated, the option to run experiments on that sensor will be disabled until calibration files have been loaded and analyzed. A number of such dependencies exist and can be inferred from the dashed green data transfer arrows in Fig. 5. The primary VI includes a display which indicates the state of all dependencies for the working sensor. This allows the user to ascertain the work to be done as soon as the sensor is loaded.

D. Dynamic Transmission Electron Microscope

The dynamic TEM is a modified JEOL 2000FX transmission electron microscope in which the conventional electron gun has been replaced with a laser-driven Ta photocathode described previously[17]. Electrons are generated by bombarding the photocathode with a high-energy ultraviolet laser. This laser is shaped using an arbitrary-waveform generator and complex optics to obtain a pulse which, when applied to the photocathode, delivers an approximately constant

electron flux with beam currents as high as several mA for times ranging from 30 ns to 500 ns. Images are acquired on a single-electron-sensitive CCD detector. During the experiment the detector is set to acquire data for a long time relative to the electron pulse (typically 1 second), so the temporal resolution is wholly determined by the duration of the electron pulse. Depending on the phenomenon to be observed the DTEM can be configured to capture time-resolved electron images or electron diffraction patterns. It is also outfitted with a high-energy "pump" laser which can be used to heat a region of the sample locally and initiate the reaction to be studied. This laser is deactivated when operating in nanocalorimetry + DTEM mode since the nanocalorimeter is used to heat the sample and initiate any reactions.

For *in situ* nanocalorimetry experiments, the most useful results are obtained when the DTEM is operated in electron diffraction mode with a relatively large selected area aperture (≈ 0.55 µm^2) and the maximum pulse time (500 ns). Since the sample is uniformly heated there are few meaningful contrast changes visible when operated in plan-view imaging mode; this approach differs from previous work[33] where a reaction front would traverse the sample and could provide an image showing the unreacted material, the reaction front, and the post-reaction material. On the other hand, operating in diffraction mode allows us to analyze the crystal structure of the sample in the selected area as it evolves or transforms. The maximum pulse length is chosen because it maximizes the number of electrons in the pulse and improves the signal-to-noise ratio of the image/diffraction pattern. While nanocalorimetry experiments are very fast compared to conventional thermal analysis experiments, a few milliseconds is still orders of magnitude longer than the 500 ns maximum pulse time of the DTEM electron source. Since the electron pulse is essentially instantaneous on the timescale of the reaction in the sample, there is no precision lost by using the maximum pulse time.

E. Timing and Synchronization

Synchronization between the DTEM and nanocalorimetry system is critical if intermediate states during the nanocalorimetry experiment are to be successfully captured. When running, the DTEM photocathode drive laser is continuously pulsed at a 10 Hz repeat rate. Any one of these pulses is capable of generating an electron pulse for imaging. In order to choose just one of the pulses to illuminate the sample, a fast shutter is introduced between the cathode laser optics and the DTEM photocathode. During an experiment, the detector acquires for 1 s and the fast shutter

11

opens briefly during this time to allow a single laser pulse onto the photocathode. In standard DTEM experiments, where the reaction is initiated by a sample pump laser and lasts much less than 100 ms, it is sufficient to control the delay time between the sample pump laser and the cathode laser to select the sample state that is imaged. In contrast, typical nanocalorimeter experiments last 10's to 100's of ms, and an additional complication occurs when the particular state to be imaged is not within the first 100 ms of the experiment. In this case a more elaborate synchronization scheme must be used as described below.

There are two requirements for an image to be acquired at a particular time during a nanocalorimetry experiment. The first is that a cathode laser pulse is available at that time. Since pulses of the cathode laser occur on a fixed "schedule" every 100 ms, the only way to achieve this is to make the cathode laser clock the reference signal for the entire system and trigger the nanocalorimetry experiment to start at an appropriate time relative to this reference. For example, to acquire an image at t = 170 ms relative to the start of the nanocalorimetry experiment the heating pulse would be initiated 70 ms prior to the next "tick" of the cathode laser clock (30 ms *after* the previous pulse). Electron pulses will then be available for imaging at 70 ms, 170 ms, 270 ms, etc. The second requirement is that no pulses other than the one at the time of interest are allowed into the column – otherwise the detector (acquiring for a full second) would overlay multiple images of the sample in different states.

The timing scheme developed to meet these requirements is shown schematically in Fig. 6. The 10 Hz reference signal indicating pulses of the cathode laser system is shown at the top in Fig. 6a. Requirement #1 is met by using a delay generator to produce a delayed version of the cathode laser clock (Fig. 6b) that triggers the start of heating and signal acquisition on the nanocalorimetry system. The delay is adjusted whenever a different time during the experiment is to be studied. Requirement #2 is satisfied by giving the nanocalorimetry system control of the cathode laser fast shutter. A separate output channel is configured to send a "shutter open" signal a short time before the event of interest and a "shutter close" signal a short time later as shown in Fig. 6c. This ensures the exclusion of all imaging pulses other than the one at the time of interest.

III. *In Situ* Investigation of Aluminum Melting

Melting experiments are a common metric by which nanocalorimetry systems are assessed. They are convenient because there is a single thermodynamic event (melting), it occurs at a well-defined temperature (the melting temperature), and a range of temperatures can be tested by choosing different elements or compounds with appropriate melting points. Melting experiments can also be conducted using a wide range of heating rates without altering the heat of fusion. This makes them a good standard for assessing nanocalorimeter performance at high heating rates, as opposed to more complex reactions which might proceed differently depending on heating rate. Since the *in situ* nanocalorimetry system is intended to measure reactions up to ≈ 1000 K, we chose to conduct the preliminary tests on aluminum thin films. While aluminum's melting temperature of 933 K is relatively high compared to the melting points of more standard calibration metals (In, Bi, and Sn), it is within the range of the optical calibration technique used[31], is less likely to result in chamber contamination, and allows us to assess performance over a larger fraction of the nanocalorimeter's temperature range.

A sample was deposited by electron-beam evaporation (Denton Infinity 22) consisting of 50 nm of Al (target purity 99.999 %) onto the backside of nanocalorimeter sensors fabricated using Design C (see Table I). A shadow mask was used to limit the deposition to the active area of the device. To prevent oxidation or reaction with the silicon nitride, the Al thin film was capped on both sides by 10 nm of Al_2O_3, also deposited by e-beam evaporation without breaking vacuum. The film thickness during deposition was controlled by a quartz crystal thickness monitor. Each iteration of the heating experiment consisted of two steps: (1) pseudo-constant-rate heating at 10^4 K/s (target) for 80 ms (see Appendix A for a description of this heating program), and (2) free cooling for 200 ms (a small current must be applied to be able to record the resistance and hence temperature, but it is much less than the currents used for heating). Since the experiments were conducted in vacuum the dominant mechanism for heat loss throughout the experiment was thermal radiation (conduction also contributes but its effects are comparably minor within the well-insulated measurement area). As described above, heating was initiated at a pre-defined time prior to the next DTEM imaging pulse so that a DTEM diffraction pattern was acquired during the heating pulse. By performing multiple iterations of the heating experiment and varying the time between initiation and imaging, diffraction patterns were collected at a range of

13

temperatures before, during, and after the melting event. To maximize resolution in the diffraction pattern the electron beam was spread and a $\approx$ 0.55 μm^2 selected-area aperture was used to select a region in the central TEM window on the sensor (see Fig. 2b). The same sensor and heating waveform were used for all experiments, and the same region of the sample was characterized throughout. The current sense resistance was 25 Ω for these experiments.

Typical results from the nanocalorimetry system during one heating pulse are shown in Fig. 7. The raw data was smoothed by a 1:64 downsampling, so the displayed data has an effective sampling rate of 3.125 kHz. Fig. 7a shows the evolution of temperature with time. The temperature increases at a roughly constant rate except for an inflection at $\approx$ 66 ms indicating the melting of aluminum. This event is more pronounced in Fig. 7b, which shows the heating rate (time derivative of temperature) over the same time span. The melting event appears as a downward spike in the heating rate because at that time power is temporarily being used to supply the heat of fusion rather than to heat the sensor. Fig. 7c shows the applied power as a function of time as calculated by Eq. 4. Finally, the signals in Fig. 7b and Fig. 7c are combined as per Eq. 5 to calculate the total heat capacity, plotted versus temperature in Fig. 7d. Here the melting event appears as an upward spike.

Fig. 8 shows a sequence of electron diffraction patterns from the experiments. The patterns in the right-hand column were captured during the heating segment of the experiment at the times/temperatures indicated by the arrows in Fig. 7b and Fig. 7d. The patterns in the left-hand column were captured at room temperature between experiments, and are included for comparison because the grain under observation solidified in a different orientation after each experiment. The grain orientation and principal diffraction spots for each of the room temperature diffraction patterns are indicated in Fig. 8. The diffuse, radially symmetric intensity present in all diffraction patterns is due to scattering from the amorphous silicon nitride film.

IV. Discussion

The dashed lines on Fig. 7b show the discrepancy between the target heating rate and the true heating rate. While the heating rate appears roughly constant in Fig. 7a, it actually varies by up to 15 % around the average heating rate of 8945 K/s. This heating rate, in turn, is about 10 %

lower than the target heating rate of 10000 K/s. This illustrates the difficulty of achieving a constant heating rate in a system without feedback control, even with the complex heating pulse developed in Eq. A8. Fig. 7d shows how the enthalpy of fusion is estimated from effective heat capacity data. A baseline curve is fitted to the data everywhere except the spike associated with melting. The integral between these two curves is then the experimentally found heat of fusion for aluminum, 0.174 mJ. Using the nominal sample dimensions of 50 nm × 4 mm × 0.75 mm (estimated from the dimensions of the shadow mask used for patterning) and the density and molar mass of bulk aluminum (2.70 g/cm^3 and 26.98 g/mol respectively), we calculate the molar heat of fusion to be 11.6 kJ/mol which is about 8.3 % higher than the value reported for melting of bulk Al, 10.71 kJ/mol[34]. This difference is not surprising given the lack of means to directly measure the sample mass along with the other uncertainties in the DTEM nanocalorimetric experiment. We note that the melting point observed experimentally is 896 K, 4 % below that of pure bulk aluminum.

When combined with the nanocalorimetry data in Fig. 7, the diffraction patterns in Fig. 8 demonstrate the ability of the combined nanocalorimetry + DTEM system to resolve events both thermodynamically and structurally. Pattern A was captured 60 ms into the heating pulse. According to the nanocalorimeter (Fig. 7d) the pattern was captured prior to melting and DTEM confirms this, showing distinct $\bar{2}00$ and 200 diffraction spots persisting from the room temperature pattern. Note that spots from the (020) axis (visible in the initial pattern A') disappear upon heating. This is likely due to expansion and flexure of the silicon nitride support membrane causing the grain under observation to tilt into an off-axis position where only the (200) spots are excited. Pattern B was captured 65 ms into the heating pulse on the leading edge of the melting peak, and the reduced intensity and broadening of the diffraction peaks indicates that while still present, crystalline order in the sample is beginning to break down. Finally, pattern C was captured at the very end of the melting peak (t = 75 ms). In this case, the DTEM diffraction pattern shows no detectable crystalline diffraction spots indicating that the sample has melted. The only distinguishable feature in this diffraction pattern is from the amorphous silicon nitride, which unfortunately prevents us from detecting an analogous halo due to the presence of molten aluminum.

V.   Future Work

The aluminum melting experiments presented above effectively demonstrate the ability of the *in situ* nanocalorimetry system to synchronize nanocalorimeter experiments with the DTEM and correlate microstructural and thermodynamic information about the sample. In its present state, this system is already capable of characterizing a wide range of materials phenomena. A forthcoming paper will document initial results in a study examining the effects of heating rate on the intermediate phases formed during the reaction of Ni and Al, and experiments on other reactive materials including thermites and nano-aluminum powder have also been discussed. More generally, we anticipate that the development of the *in situ* nanocalorimetry + DTEM system will impact a variety of materials fields where the interplay between thermodynamic and kinetic control is important, including nucleation and solidification, crystallization in metallic glasses, and phase change materials.

One of the greatest drawbacks to the system in its present state is that it is limited to single-shot electron imaging. While not insurmountable, this restriction means that many identical samples are required to fully characterize an irreversible reaction. Even reversible reactions, which benefit from the ability to repeatedly "pump" and "probe" the sample, take longer to characterize with the single-shot approach. A so-called "movie mode" for the DTEM has been developed where a sequence of 9 or 16 images can be captured during a single experiment. Unfortunately, due to limitations in the current laser optics this mode cannot at present be applied on the longer timescales typical of nanocalorimetry experiments. Extending this capability to the millisecond timescale would dramatically improve the throughput of future *in situ* nanocalorimetry experiments.

Other improvements are possible in the area of sensor design. One of these improvements is detailed in section IIA, where we found that reducing the size of the holes in the Pt heater from 100 μm squares (Design C) to 20 μm squares (Design D) resulted in significantly enhanced temperature uniformity. In addition, we anticipate that reducing the thickness of the silicon nitride support membrane or eliminating it entirely in the imaging region would noticeably improve image quality by eliminating the amorphous background. We are currently developing a process to introduce small holes in the silicon nitride membrane for this purpose.

VI.   Conclusions

By combining nanocalorimetry and dynamic TEM a new high-rate *in situ* characterization tool has been developed which provides thermal and microstructural characterizations across the full range of heating rates available with nanocalorimetry, approximately 10^3 K/s to 10^5 K/s. The system consists of the DTEM, a new TEM-compatible nanocalorimeter sensor, a custom-built *in situ* nanocalorimetry holder, and a data acquisition system with accompanying software. When a synchronization scheme is established it is possible to capture DTEM images or diffraction patterns of intermediate states in the sample at any time/temperature point in a reaction and across the range of heating rates available via nanocalorimetry. This development simplifies the microstructural analysis of reactions which is essential to virtually all nanocalorimeter experiments, and provides the first opportunity to characterize *in situ* those reactions that are dependent on high heating or cooling rates.

Appendix: Functional Form for Heating Pulses

In order to achieve approximately constant heating rates in a voltage-controlled configuration without feedback, a new equation was developed to calculate the voltage waveform required for approximately constant heating rate. The objective is a constant heating rate, β, defined as the ratio of temperature change to pulse time:

$$\beta = \Delta T / \Delta t \tag{A1}$$

The temperature in the measurement area of the sensor is governed by the differential equation

$$C_p \dot{T} = \dot{Q}_{ext} + \dot{Q}_{rxn} - \dot{Q}_{loss} \tag{A2}$$

where C_p is the heat capacity of the measurement area, $\dot{T}$ is the heating rate dT/dt, and the three $\dot{Q}$ terms on the right-hand-side are the externally applied power, the power from any reactions on the chip, and the heat loss power, respectively. Since $\dot{Q}_{rxn}$ cannot be known *a priori*, it is assumed to be zero. This means that the computed waveform is only designed to deliver a constant heating rate in the absence of reactions on the chip. If the heating rate is constant, we can replace it with the target heating rate, β, and solve for the target applied power:

$$\dot{Q}_{ext} = C_p \beta + \dot{Q}_{loss} \tag{A3}$$

If the heat capacity and heat losses of the chip can be estimated accurately as a function of temperature, this expression gives the applied power required to maintain a constant heating rate. In order to convert it to a voltage waveform we must consider the specifics of the nanocalorimeter heating circuit. The origin of the applied power is resistive heating in the nanocalorimeter strip. This can be computed as

$$\dot{Q}_{ext} = V_{strip}(t)^2 / R_{strip}(t) \tag{A4}$$

Solving for the voltage and including the result from above, we find

$$V_{strip}(t) = \sqrt{R_{strip}(t)\left(C_p \beta + \dot{Q}_{loss}\right)} \tag{A5}$$

In order to approximate the resistance of the strip, recall that each chip is calibrated prior to use. This calibration can be used to fit a polynomial that describes the resistance of the strip at any

given temperature, $R_{\text{calib}}(T)$. We also know that, if a constant heating rate is achieved, the temperature will follow $T(t) = \beta t + T_0$, where T_0 is the ambient temperature. This gives us

$$V_{\text{strip}} = \sqrt{J \times R_{\text{calib}}(T_0 + \beta t)\left[C_p\beta + \dot{Q}_{\text{loss}}(T_0 + \beta t)\right]} \qquad \text{(A6)}$$

where the one additional modification is the factor J, equal to the ratio of the heater strip's total length to the distance between the voltage probes used to measure the resistance. J is always greater than one and has the effect of increasing the overall voltage applied. Finally, to convert the voltage drop across the strip to the total voltage which must be applied to the circuit we must consider the other loads in the circuit. In the case of the nanocalorimeter system described here, these loads are purely resistive and include the sense resistor (10 Ω – 100 Ω), a ground isolation resistor (≈ 5 Ω), and the resistance of the wires that connect the auxiliary electronics to the chip at the holder tip (≈ 30 Ω). The sum of these resistances is on the same order as the chip resistance (typically 30 Ω – 70 Ω) so the voltage across the strip will be much lower than intended unless we account for the voltage divider effect. Lumping all of the resistances other than the heater strip into an approximate value R_{other}, the voltage across the strip will be related to the total applied voltage $V(t)$ by

$$V_{\text{strip}}(t) = V(t)\frac{R_{\text{strip}}}{R_{\text{strip}} + R_{\text{other}}} \qquad \text{(A7)}$$

Solving for the total voltage and substituting from above, we finally arrive at the functional form used for constant heating rate waveforms in these experiments,

$$V(t) = \left(1 + \frac{R_{\text{other}}}{J \times R_{\text{calib}}^{\text{RT}}}\right)\sqrt{J \times R_{\text{calib}}(T_0 + \beta t)\left[C_p\beta + \dot{Q}_{\text{loss}}(T_0 + \beta t)\right]} \qquad \text{(A8)}$$

Note that here, although the voltage divider term could have been made time-dependent using the same assumptions as above, we found that a constant term based on the room-temperature resistance of the chip gave the best results. As shown in Fig. 7a and Fig. 7b, this waveform accomplishes an approximately constant heating rate. As introduced in Eq. A3, the effect of heat loss compensation is to increase the power required to heat the chip at a given rate as the temperature increases. For radiative losses, which scale with T^4, this increase can be quite dramatic as illustrated in Fig. 7c.

References

[1] S.L. Lai, G. Ramanath, L.H. Allen, P. Infante, and Z. Ma, Appl. Phys. Lett. **67**, 1229 (1995).

[2] E.A. Olson, M.Y. Efremov, and L.H. Allen, J. Microelectromechanical Syst. **12**, 355 (2003).

[3] E.A. Olson, M.Y. Efremov, Z.S. Zhang, L.H. Allen, S.L. Lai, M. Zhang, and F. Schiettekatte, Thermochim. Acta **412**, 13 (2004).

[4] P. Swaminathan, D.A. LaVan, and T.P. Weihs, J. Appl. Phys. **110**, 113519 (2011).

[5] M. Zhang, E.A. Olson, R.D. Twesten, J.G. Wen, L.H. Allen, I.M. Robertson, and I. Petrov, J. Mater. Res. **20**, 1802 (2005).

[6] R.K. Kummamuru, L. De La Rama, L. Hu, M.D. Vaudin, M.Y. Efremov, M.L. Green, D.A. LaVan, and L.H. Allen, Appl. Phys. Lett. **95**, 181911 (2009).

[7] P. Swaminathan, M.D. Grapes, K. Woll, S.C. Barron, D.A. LaVan, and T.P. Weihs, J. Appl. Phys. **113**, 143509 (2013).

[8] P.J. McCluskey and J.J. Vlassak, Scr. Mater. **64**, 264 (2011).

[9] P.J. McCluskey, C. Zhao, O. Kfir, and J.J. Vlassak, Acta Mater. **59**, 5116 (2011).

[10] J.M. Gregoire, P.J. McCluskey, D. Dale, S. Ding, J. Schroers, and J.J. Vlassak, Scr. Mater. **66**, 178 (2012).

[11] A.A. Minakov, S.A. Adamovsky, and C. Schick, Thermochim. Acta **432**, 177 (2005).

[12] J.-L. Garden, E. Château, and J. Chaussy, Appl. Phys. Lett. **84**, 3597 (2004).

[13] H. Huth, A.A. Minakov, and C. Schick, J. Polym. Sci. Part B Polym. Phys. **44**, 2996 (2006).

[14] K. Xiao, J.M. Gregoire, P.J. McCluskey, and J.J. Vlassak, Rev. Sci. Instrum. **83**, 114901 (2012).

[15] J.M. Gregoire, K. Xiao, P.J. McCluskey, D. Dale, G. Cuddalorepatta, and J.J. Vlassak, Appl. Phys. Lett. **102**, 201902 (2013).

[16] K. Xiao, J.M. Gregoire, P.J. McCluskey, D. Dale, and J.J. Vlassak, J. Appl. Phys. **113**, 243501 (2013).

[17] T. LaGrange, M.R. Armstrong, K. Boyden, C.G. Brown, G.H. Campbell, J.D. Colvin, W.J. DeHope, A.M. Frank, D.J. Gibson, F.V. Hartemann, J.S. Kim, W.E. King, B.J. Pyke, B.W. Reed, M.D. Shirk, R.M. Shuttlesworth, B.C. Stuart, B.R. Torralva, and N.D. Browning, Appl. Phys. Lett. **89**, 044105 (2006).

[18] T. LaGrange, G.H. Campbell, B.W. Reed, M.L. Taheri, J.B. Pesavento, J.S. Kim, and N.D. Browning, Ultramicroscopy **108**, 1441 (2008).

[19] B.W. Reed, T. LaGrange, R.M. Shuttlesworth, D.J. Gibson, G.H. Campbell, and N.D. Browning, Rev. Sci. Instrum. **81**, 053706 (2010).

[20] T. LaGrange, G.H. Campbell, P.E.A. Turchi, and W.E. King, Acta Mater. **55**, 5211 (2007).

[21] T. LaGrange, G.H. Campbell, J.D. Colvin, B.W. Reed, and W.E. King, J. Mater. Sci. **41**, 4440 (2006).

[22] J.T. McKeown, A.K. Kulovits, C. Liu, K. Zweiacker, B.W. Reed, T. LaGrange, J.M.K. Wiezorek, and G.H. Campbell, Acta Mater. **65**, 56 (2014).

[23] M.K. Santala, B.W. Reed, S. Raoux, T. Topuria, T. LaGrange, and G.H. Campbell, Appl. Phys. Lett. **102**, 174105 (2013).

[24] M.K. Santala, B.W. Reed, S. Raoux, T. Topuria, T. LaGrange, and G.H. Campbell, Phys. Status Solidi **249**, 1907 (2012).

[25] M.K. Santala, B.W. Reed, T. Topuria, S. Raoux, S. Meister, Y. Cui, T. LaGrange, G.H. Campbell, and N.D. Browning, J. Appl. Phys. **111**, 024309 (2012).

[26] A. Kulovits, J.M.K. Wiezorek, T. LaGrange, B.W. Reed, and G.H. Campbell, Philos. Mag. Lett. **91**, 287 (2011).

[27] L. Nikolova, T. LaGrange, B.W. Reed, M.J. Stern, N.D. Browning, G.H. Campbell, J.-C. Kieffer, B.J. Siwick, and F. Rosei, Appl. Phys. Lett. **97**, 203102 (2010).

[28] G.H. Campbell, T. LaGrange, J.S. Kim, B.W. Reed, and N.D. Browning, J. Electron Microsc. (Tokyo). **59 (Supp.)**, S67 (2010).

[29] J.S. Kim, T. Lagrange, B.W. Reed, M.L. Taheri, M.R. Armstrong, W.E. King, N.D. Browning, and G.H. Campbell, Science **321**, 1472 (2008).

[30] J.S. Kim, T. LaGrange, B.W. Reed, R. Knepper, T.P. Weihs, N.D. Browning, and G.H. Campbell, Acta Mater. **59**, 3571 (2011).

[31] P. Swaminathan, B.G. Burke, A.E. Holness, B. Wilthan, L. Hanssen, T.P. Weihs, and D.A. LaVan, Thermochim. Acta **522**, 60 (2011).

[32] B.L. Zink, B. Revaz, J.J. Cherry, and F. Hellman, Rev. Sci. Instrum. **76**, 024901 (2005).

[33] T. LaGrange, B.. Reed, M.. Santala, J.. McKeown, A. Kulovits, J.M.K. Wiezorek, L. Nikolova, F. Rosei, B.J. Siwick, and G.H. Campbell, Micron **43**, 1108 (2012).

[34] J.A. Dean and N.A. Lange, *Lange's Handbook of Chemistry*, 15th ed. (McGraw-Hill, 1999), p. 1424.

Tables

Table I: Specifications for the four heater geometries investigated by finite element modeling. The size of the measurement area is characterized by the length between the voltage probes. The heater width is equal for all designs (0.5 mm), and the total size of the silicon nitride window is constant. Designs C and D employ square holes; the hole size listed is the length of one side of the square.

Design Name	Length of Measurement Area	Hole Size
Design A	5.7 mm	none
Design B	3.7 mm	none
Design C	3.7 mm	100 μm
Design D	3.7 mm	20 μm

Table II: Material properties used for finite element simulation of temperature distribution in nanocalorimeter sensors. See Fig. 3 for electrical conductivity of Pt.

Material	Thermal Conductivity (W m^{-1} K^{-1})	Heat Capacity (J kg^{-1} K^{-1})	Density (g cm^{-3})	Emissivity (dimensionless)
Pt	71.6	133	21.45	$0.186 + (6.48 \times 10^{-5})T$
SiN$_x$	3.2	750	3.100	0

Figure Captions

Fig. 1 – Schematic diagram of the combined nanocalorimetry + DTEM system highlighting the interactions and connections between the component systems.

Fig. 2 – The nanocalorimeter sensor used in these experiments: (a) a side-view schematic (not to scale), and (b) a top-view micrograph showing 100 micron square holes for electron imaging.

Fig. 3 – Finite element modeling results showing the steady-state temperature distribution of nanocalorimeter sensors under constant current. At left are histograms of temperature values (from a uniformly spaced grid to avoid mesh density bias) comparing the temperature distribution for the four designs. The vertical dashed line indicates the average temperature in all simulations, 939 K. At right are contour plots of the steady state temperature distribution. The dashed boxes indicate the measurement area for each design. In the upper-right quadrant of each plot the mesh geometry is shown. This is the only quadrant that was simulated, with the remaining three inferred from symmetry. The scale of the contour plots is limited to the range from 920 K to 960 K in order to highlight temperature variations around the mean.

Fig. 4 – Photographs of the custom-built TEM holder developed for *in situ* nanocalorimetry: (a) overview of the entire holder, (b) close-up of breakout box with cover removed to show auxiliary electronics, (c) close-up of sensor mounting region with sensor and clamp removed, showing spring-pin electrical connections for face-down mounting, and (d) close-up of mounting region with sensor (visible through hole) and clamp installed.

Fig. 5 – High-level diagram depicting the flow of program calls and data within the nanocalorimetry operations software. All calls are initiated from the entry-point program "Nanocalorimeter Operations" and include all information about the working chip needed for the sub-programs to perform their tasks.

Fig. 6 – Schematic diagram illustrating the synchronization scheme between the nanocalorimetry system and the dynamic TEM. The cathode laser clock serves as the reference signal by which the nanocalorimetry experiment is initiated after some delay. The extra cathode laser pulses are ignored because the fast shutter is only opened briefly at the time of interest.

Fig. 7 – Characteristic nanocalorimetry results for the heating segment of the aluminum melting experiment: (a) temperature vs. time, (b) heating rate vs. time, (c) applied power vs. time, and (d) net heat capacity vs. temperature. The labeled arrows in (b) and (d) indicate the times/temperatures at which DTEM diffraction patterns were captured during the heating scan, and the shaded area in (d) represents the experimental heat of fusion.

Fig. 8 – Several single-crystal diffraction patterns taken from one grain of the aluminum film during the melting experiments. The patterns on the left were taken at room temperature, while those on the right were taken at different times during the heating segment of the experiment. The time and temperature is given for each pattern on the right, and the crystal orientation and principal diffraction spots are labeled for each pattern on the left. These points are also indicated in the melting curves shown in Fig. 7b and Fig. 7d. All images are displayed with the same brightness and contrast.
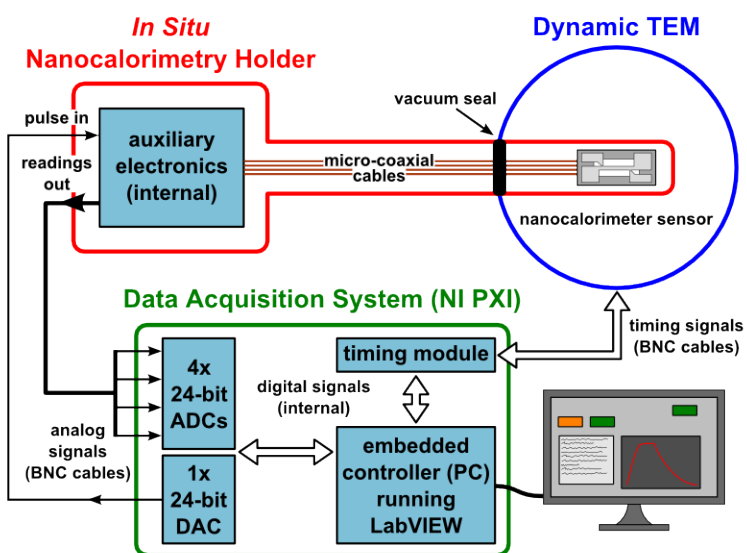
Figures

Fig. 1 – Schematic diagram of the combined nanocalorimetry + DTEM system highlighting the interactions and connections between the component systems.
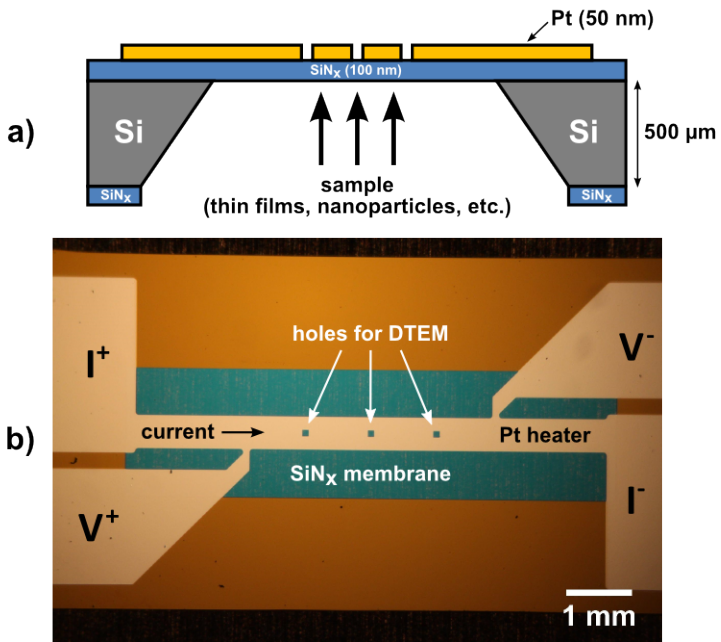
Fig. 2 – The nanocalorimeter sensor used in these experiments: (a) a side-view schematic (not to scale), and (b) a top-view micrograph showing 100-micron square holes for electron imaging.
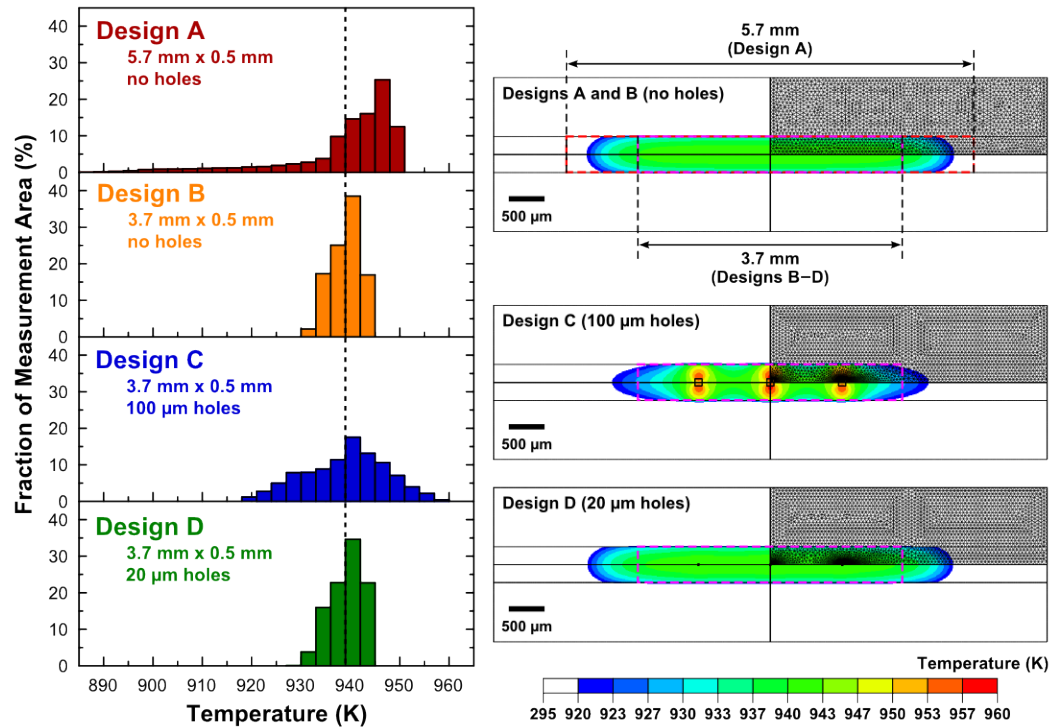
Fig. 3 – Finite element modeling results showing the steady-state temperature distribution of nanocalorimeter sensors under constant current. At left are histograms of temperature values (from a uniformly spaced grid to avoid mesh density bias) comparing the temperature distribution for the four designs. The vertical dashed line indicates the average temperature in all simulations, 939 K. At right are contour plots of the steady state temperature distribution at the conclusion of each simulation. The dashed boxes indicate the measurement area for each design. In the upper right quadrant the mesh geometry used in each simulation is shown. This is also the only quadrant that was simulated, with the remaining three inferred from symmetry.
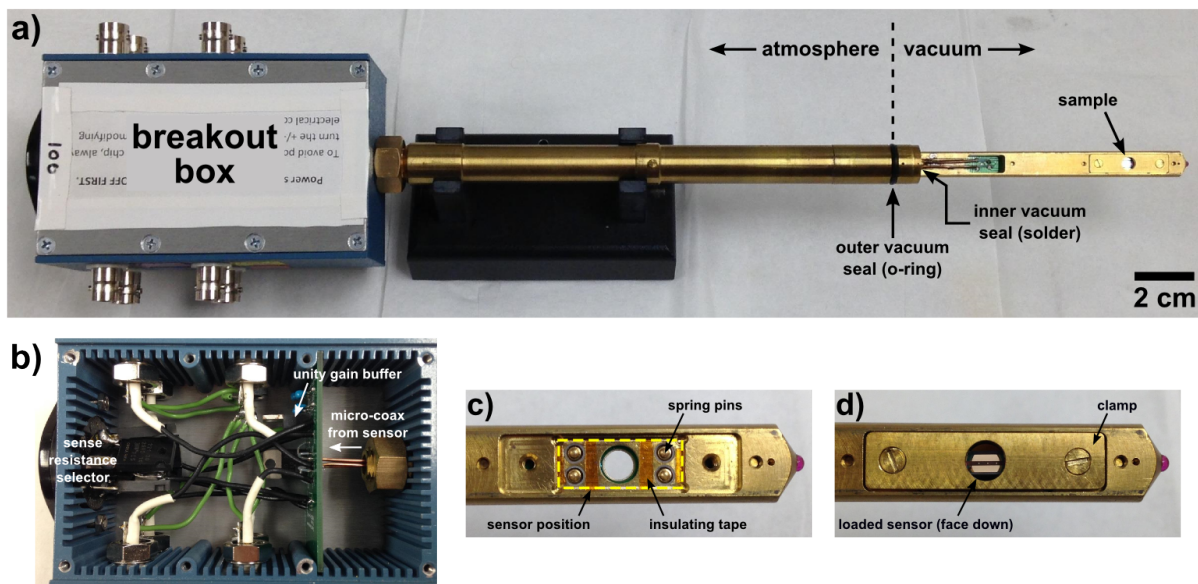
Fig. 4 – Photographs of the custom-built TEM holder developed for *in situ* nanocalorimetry: (a) overview of the entire holder, (b) close-up of breakout box with cover removed to show auxiliary electronics, (c) close-up of sensor mounting region with sensor and clamp removed, showing spring-pin electrical connections for face-down mounting, and (d) close-up of mounting region with sensor (visible through hole) and clamp installed.
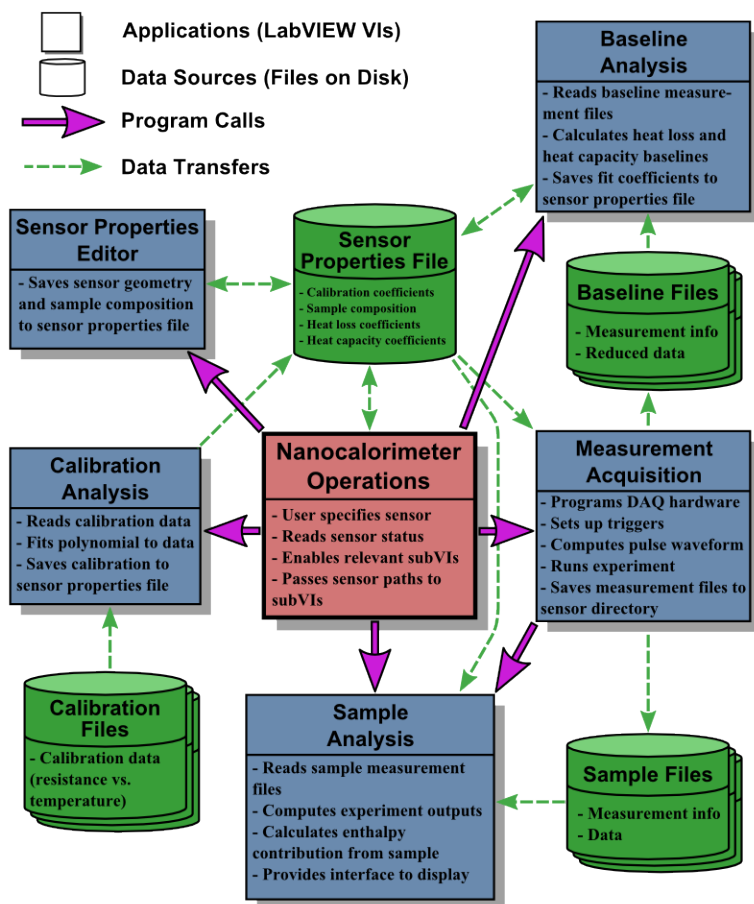
Fig. 5 – High-level diagram depicting the flow of program calls and data within the nanocalorimetry operations software. All calls are initiated from the entry-point program "Nanocalorimeter Operations" and include all information about the working chip needed for the sub-programs to perform their tasks.
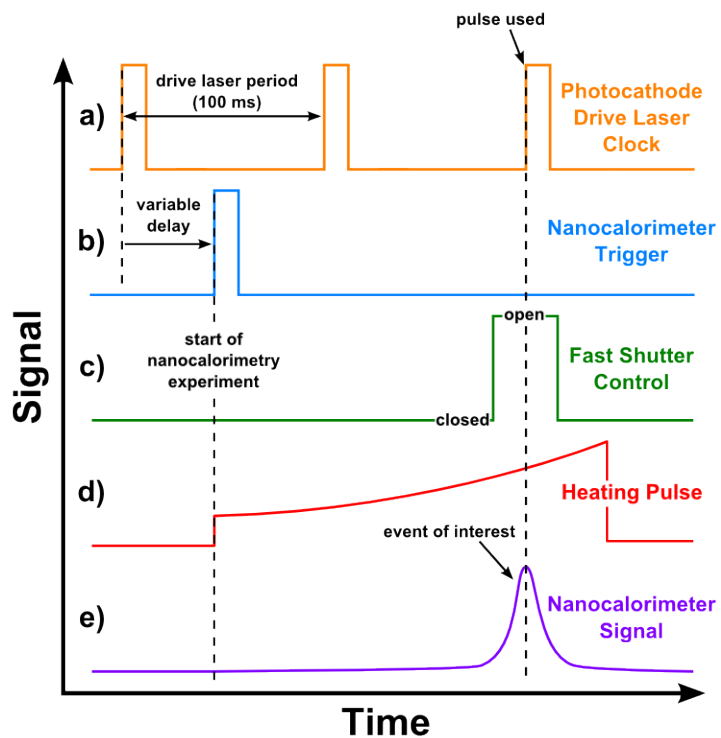
Fig. 6 – Schematic diagram illustrating the synchronization scheme between the nanocalorimetry system and the dynamic TEM. The photocathode laser clock serves as the reference signal by which the nanocalorimetry experiment is initiated after some delay. The extra cathode laser pulses are ignored because the fast shutter is only opened briefly at the time of interest.
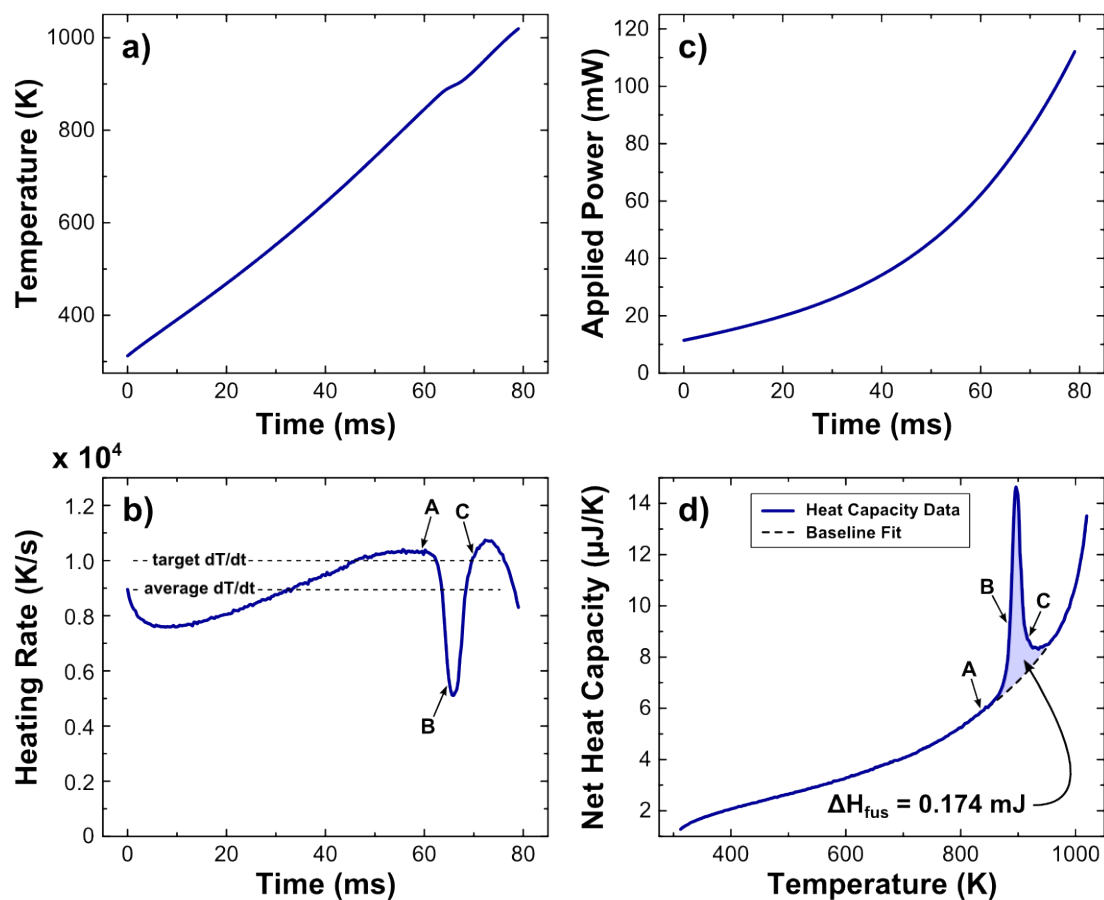
Fig. 7 – Characteristic nanocalorimetry results for the heating segment of the aluminum melting experiment: (a) temperature vs. time, (b) heating rate vs. time, (c) applied power vs. time, and (d) net heat capacity vs. temperature. The labeled arrows in (b) and (d) indicate the times/temperatures at which DTEM diffraction patterns were captured during the heating scan, and the shaded area in (d) represents the experimental heat of fusion.
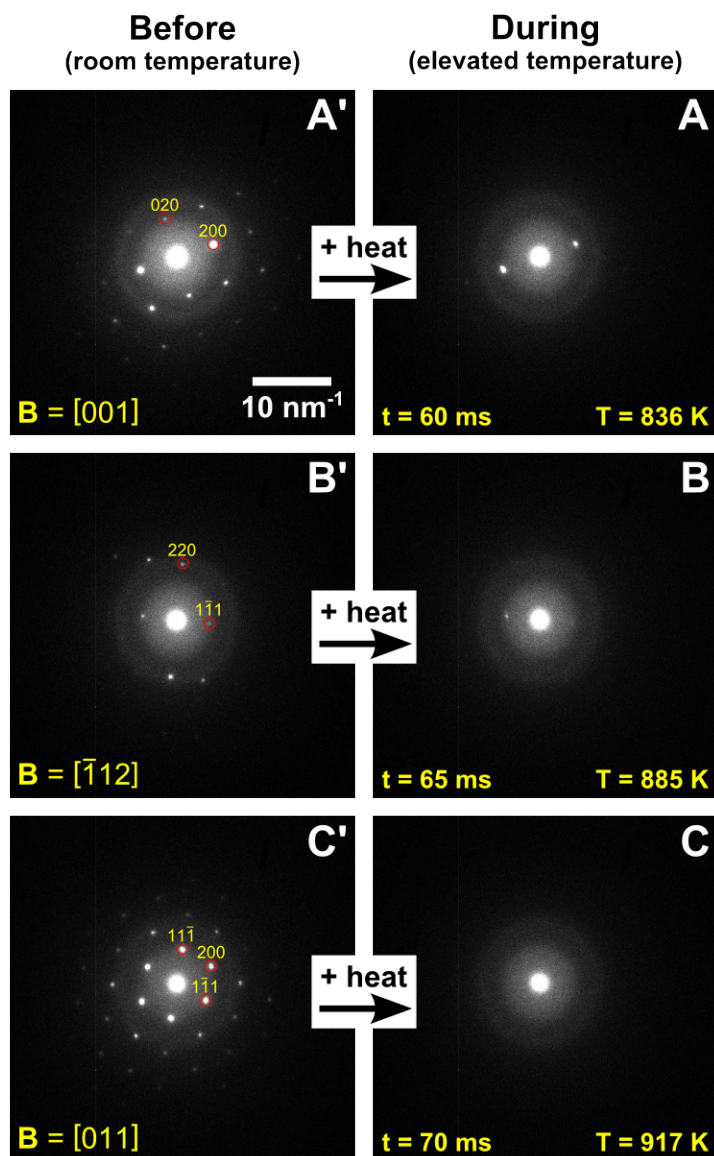
Fig. 8 – Several single-crystal diffraction patterns taken from one grain of the aluminum film during the melting experiments. The patterns on the left were taken at room temperature, while those on the right were taken at different times during the heating segment of the experiment. The time and temperature is given for each pattern on the right, and the crystal orientation and principal diffraction spots are labeled for each pattern on the left. All images are displayed with the same brightness and contrast.